ARTICLE

Check for updates

Fertile upper mantle peridotite xenoliths indicate no wholesale destruction of cratonic root in East Asia

Vinod O. Samuel[1], Sanghoon Kwon[1], Yirang Jang [2✉], Youngwoo Kil[3], M. Santosh[4,5,6], Chaewon Park [1] & Keewook Yi[7]

A major question in geodynamic evolution of the Earth is whether the continental keel evolved geochemically or were delaminated and replaced by a new mantle. Here we present direct evidence for the geochemical evolution of continental keel from lherzolite xenoliths preserved in the Cenozoic alkali basalts from Jeju Island, Korea. Our findings, using detailed petrography and geochemical methods, reveal distinct textures and compositional changes (represented by olivine with magnesium number 91–87, 86–61 respectively) of two stages of geochemical alteration. The first stage involved a parental kimberlite melt that penetrated during the Paleozoic, and the second was caused by alkali basalt during Cenozoic. Our findings suggest that the Archean depleted harzburgitic upper mantle partially evolved to lherzolitic through interaction with melts/fluids that originated from the deep mantle, implying no wholesale delamination of the upper mantle root of East Asian continents.

[1] Department of Earth System Sciences, Yonsei University, Seoul 03722, Republic of Korea. [2] Department of Earth and Environmental Sciences, Chonnam National University, Gwangju 61186, Republic of Korea. [3] Department of Energy and Resources Engineering, Chonnam National University, Gwangju 61186, Republic of Korea. [4] School of Earth Sciences and Resources, China University of Geosciences Beijing, Beijing 100083, China. [5] Department of Earth Science, University of Adelaide, Adelaide, SA 5005, Australia. [6] Yonsei University Frontier Lab, Yonsei University, Seoul 03722, Republic of Korea. [7] Division of Earth and Environmental Sciences, Korea Basic Science Institute, Chungbuk 28119, Republic of Korea. ✉email: yirang@jnu.ac.kr

Earth as an evolving planet continues to be in a non-equilibrium dynamic state since its formation[1]. During its evolution, the planet witnessed large-scale and active lithospheric processes, such as rifting, collision, and subduction[2,3]. These processes extracted the continental crust from the mantle, leaving a residual depleted peridotite in the upper mantle[4]. Such depleted residues form the roots of the oldest cratons and have a dominantly harzburgitic composition probably due to the high degree of melting to generate komatiite or oceanic crust in the Archean[4,5]. The depleted residual harzburgite in Archean Cratons (such as in Canada[4], North America[4], South Africa[6], Siberia[7], North China[8,9] etc.) has olivine grains with the highest Mg number (Mg# ~92–93) compared to younger depleted peridotites in the mobile belts and in the ocean floor worldwide (abyssal peridotites; Mg# 88–89)[4,5,10]. The younger depleted peridotites with relatively low-Mg olivine (with respect to modal olivine percentage) define an 'oceanic trend' compared to high-Mg olivine-bearing Archean depleted peridotites[10]. This difference in remnant peridotite records throughout Earth's history provides one of the prominent traces of the geochemical changes in the upper mantle peridotite composition since the Archean[4,5,10]. In addition to this, un-depleted (relatively fertile) fragments of mantle rocks (xenoliths) hosted by intraplate basalts, lamproites, and kimberlites that penetrated continents during different times in Earth's history show striking mineralogical and geochemical variations[11–13]. The depleted harzburgitic xenoliths are mainly replaced by fertile lherzolite xenoliths (examples include those from South Africa[6] and Siberia[7], North China[8,9], North America[11]etc.). One of the important mineralogical features is the presence of clinopyroxene in the fertile lherzolite compared to its absence in Archean-depleted harzburgite[8–14]. Related geochemical variations in fertile lherzolites include high Ca activity, low Mg# of olivine, enrichment in elements extracted during partial melting, Fe enrichment etc.[8–14]. A multitude of geochemical studies on such intraplate depleted and fertile xenolith samples along with geophysical and numerical modeling studies suggest that these variations (both mineralogical and geochemical) could probably represent mechanical replacement processes such as large-scale destruction or delamination, or dripping or peeling-off of depleted mantle roots of continents[8,9,11,13–17]. This would suggest an episodic process of upper mantle replacement during which cold light viscous residues of the older mantle eventually destroy, drip, peel-off or delaminate to the lower mantle, and a new hot fertile mantle would be emplaced. Such processes are believed to cause the destruction of the mantle keel beneath old cratons (typically older than 2 Ga) and destabilize them during major subduction-collision processes, eventually leading to continental break-up[13–17].

The xenoliths derived from intracontinental basalts and kimberlites (representing the thick-light-cold-roots of cratons and mobile belts) are the most important global proxies for upper mantle processes. Peridotite xenoliths suitable for Re-Os dating show Archean (2.6 to 2.9 Ga) age for a depleted lithospheric mantle beneath several well-studied cratons such as North America, South Africa, and East Asia[11–13]. For example, in East Asia, the North China Craton preserves Archean-depleted harzburgitic mantle xenoliths in the Ordovician kimberlite intrusions compared to lherzolitic xenoliths in younger Mesozoic–Cenozoic alkali basalt intrusions[8,9,14]. Compared to depleted harzburgites, the age of the fertile lherzolites are puzzling due to the inhomogeneities in the isotope patterns, with multiple distributions with peaks at ca. 1.8 Ga–0.13 Ga[14]. Such disruptions are interpreted to indicate whole-scale loss of the Archean lithospheric mantle due to delamination, and simultaneous substitution of a younger lherzolitic mantle, and reflect the inhomogeneities of Re-

Os isotope distribution in the deeper source mantle[8,9,14]. The North and South China Cratons were welded together during the Permo-Triassic collisional processes, and it has been suggested that the collisional process could have exerted a major role in delaminating the old lithospheric mantle[14]. However, there is a possibility that these mineralogical variations and isotopic inhomogeneities could also represent geochemical variations in the upper mantle rather than a wholescale destruction.

Similar to mineralogical and geochemical variations observed in the xenoliths from the North China Craton, those in the Korean Peninsula also display both depleted harzburgite and fertile lherzolite compositions[18,19]. Re-Os dating of depleted harzburgite xenoliths in the Korean Peninsula yielded melt extraction age of 1.9–2.1 Ga[19]. These ages indicate that much older harzburgites could be present in the continental roots and have not been sampled yet[19]. Similar to lherzolite xenoliths in the North China Craton, fertile lherzolite xenoliths in the Korean peninsula also show disruptions in their Re-Os age patterns. These variations are attributed to delamination of the upper mantle during multiple times, and to isotope inhomogeneities in the mantle source from which these xenoliths were derived[19].

Xenoliths are important direct evidence that could provide clues regarding the mechanism of mantle replacement. Although they show geochemical and mineralogical variations, the main mechanism of mantle replacement still remains an outstanding question. In this study, we present robust evidence for orthopyroxene replacement reactions preserved in a fertile lherzolitic xenolith hosted by alkali basalts from Jeju Island in the Korean Peninsula. We also present data on geochemical and oxygen isotope variations. Several previous studies assumed that such mineral replacement reactions might be absent in the xenolith samples[18]. However, our detailed study using petrological techniques and elemental mapping using electron micro-probe revealed important textural relations that are crucial in understanding the geochemical evolution of the upper mantle. Our study suggests that lherzolite composition is overprinted on some of the oldest harzburgites in the upper mantle. This geochemical evolution occurred during the pervasive chemical alteration by kimberlite and alkali-basalt melts that originated at different times from the deep mantle. Our results suggest that the upper mantle root of East Asian continents is relatively unbroken, and has geochemically evolved from a depleted harzburgite to fertile lherzolite composition since the Archean. These geochemical alterations would also account for the inhomogeneities observed in the Re-Os isotope distribution. Our study has implications on the stability of continental crust, nature, and composition of fluids in the deep mantle, and also suggests that the deeper mantle evolves through geochemical mixing with the subducting oceanic lithosphere (with no contribution of continental roots) through time.

Results

Lherzolite xenoliths from Jeju Island, South Korea. The South Korean Peninsula is located in a central domain with the North China Craton in the north, the South China Craton in the west, the Pacific Plate subduction zone and Japanese islands in the East, and Philippine subduction zone in the south (Fig. 1a). The peninsula is dominantly composed of Archean to Paleoproterozoic felsic magmatic basement rocks, and felsic-mafic-ultramafic rocks that formed through the Proterozoic to the Phanerozoic[20,21]. The latest intraplate volcanism in the peninsula generated alkali basaltic eruptions in multiple localities similar to those in many parts of east and south-east Asia[18,22]. These basaltic lavas carry several peridotite xenoliths such as in the Baengnyeong Island, Jogokni, and Jeju Island. We collected
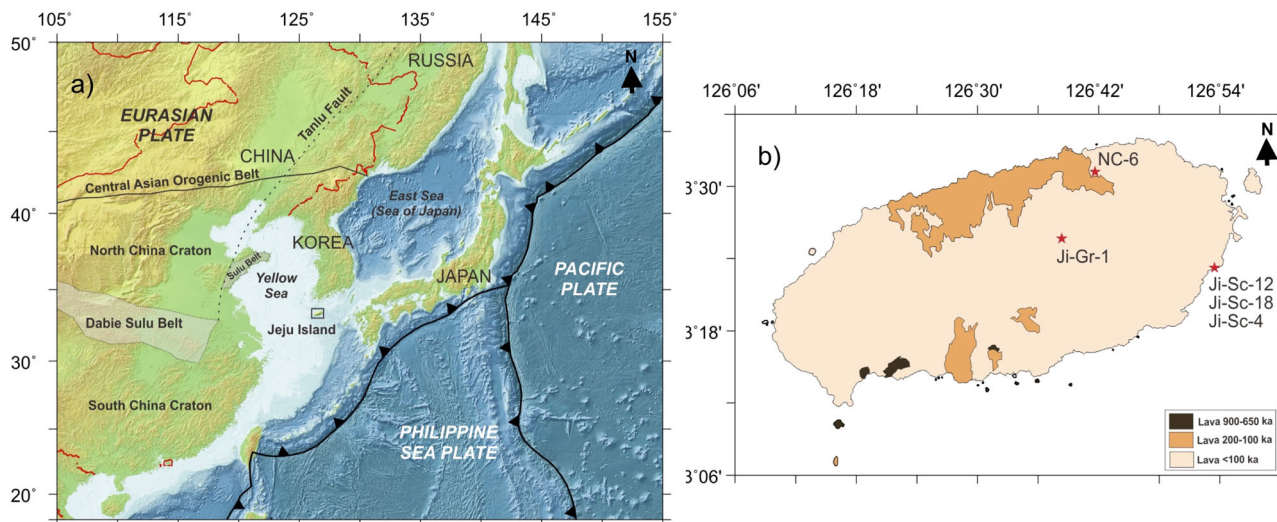
Fig. 1 Regional tectonic settings and Jeju Island geology. a regional tectonic, and **b** Jeju Island Geology maps produced using Generic Mapping Tools (GMT V5.3.3)[65]; elevation data extracted from the GEBCO_2023 Grid[66]; The Jeju Island geology is redrawn after previous study[67]. Sample locations are also shown in the geology map of Jeju Island.

xenolith samples for this study from Jeju Island, a mainly volcanic island located at the south-western part of the continental shelf of the Korean Peninsula (Fig. 1a, b). This island is mainly composed of Mesozoic (Jurassic– Cretaceous) granitic basement penetrated by alkali to trachyte basaltic eruptions from *ca*. 1.2 Ma – 1570 AD[22–25]. None of these basaltic outcrops have undergone any post eruptive tectonic deformation, and they preserve their original massive form (Supplementary Fig. 1)[18,19,22].

We selected five representative spinel lherzolite peridotite xenolith samples from Jeju Island for this study. Sample numbers, locations, field photographs, and xenolith photographs are provided in Fig. 1, Supplementary Figs. 1, 2, and Supplementary Table 1. Thin-section photographs, backscattered electron (BSE) images, and Mg compositional maps of the whole thin-section of all samples are provided in the Fig. 2, and Supplementary Fig. 3. All the samples are composed of olivine, clinopyroxene, orthopyroxene and minor spinel. We have divided our samples into two groups based on degree of alteration of these samples by the host alkali basalt (details are given in the sections below). Group 1 xenoliths are least altered by the host alkali basalts, and Group 2 xenoliths are extensively altered within the xenolith by interaction with the host alkali basalt. The Group 1 xenolith samples are characterized by large size of more than 5 cm × 5 cm. They show no indication of interaction with host alkali basalt at the core of the xenoliths, but show alteration (e.g. Fe enrichment) at their rims (Fig. 2a–c, and Supplementary Fig. 3). Samples Ji-Sc-18, Ji-Sc-12, Ji-Sc-4 belong to this group. Extensively altered xenoliths (Group 2) are characterized by smaller size of less than 2 cm × 2 cm, and the host alkali basalt infiltrated deep inside these samples through cracks in the xenoliths (Fig. 2d, e, and Supplementary Fig. 3). These interactions are recognized by extensive enrichment of Fe well within the xenolith (please see details below). Sample numbers NC-6 and Ji-Gr-1 belong to this group.

Harzburgite to lherzolite: mineral replacement reactions. We investigated the mineral mode, grain size, and textures of all the xenolith samples using optical microscope and electron microprobe. We have also performed extensive electron microprobe elemental mapping of all the xenolith samples. Based on our observations, we divide the petrological descriptions into three sections: core of the least altered xenoliths, rim of the least altered xenoliths, and the extensively altered xenoliths.

Mineralogy and textures at the core of the least altered (Group 1) xenoliths: In the core of the least altered samples olivine, orthopyroxene, and clinopyroxene show 2–3 mm size (Fig. 2 and Supplementary Figs. 3 and 4). Average mineral modes calculated from the three Group 1 samples show 66% olivine, 21% orthopyroxene, and 13% clinopyroxene (mineral percentage for the separate samples (by counting the pixels of different colors) are shown in a respective thin-section map in Fig. 2. Optical microscope parallel and crossed nicol images reveal the pristine nature of all the mineral grains without any deformation features such as penetrative foliation, lineation, or any deformation bands in and among the minerals, except for some kink bands in olivine and orthopyroxene (which is similar to observations in previous studies on the xenoliths from Jeju Island[18]) (Supplementary Fig. 4).

Mg, Ca compositional imaging of representative domains in the Group 1 samples (Figs. 2, 3) clearly fingerprint features of orthopyroxene transformation to clinopyroxene, and the formation of new olivine grains. Henceforth, these (orthopyroxene, olivine, and clinopyroxene) minerals at core of the xenoliths are termed as primary minerals. In such an area (Fig. 3a–e), from left to right, there is a gradual transition of Mg composition in olivine grains (yellow to red). The olivine grains with lowest Mg values are near the area that is enriched in orthopyroxene, and olivine grains with high Mg occur further to the right. Slight changes in the Mg composition (0.87–0.9) from left to right characterizes the reaction zone (X1–X4 areas in Fig. 3a; Supplementary Data 1-sample number- Ji-Sc-4), where olivine grains have 2–3 mm size (Fig. 3a, b). This reaction zone has pockets of clinopyroxene (blue) and orthopyroxene (green). An enlarged map of such an area (Fig. 3c) shows that partial alteration of orthopyroxene to clinopyroxene leaves relict orthopyroxene on one edge. Such thin relict orthopyroxene represents the leftover from reactions. Boundaries of clinopyroxene with olivine and orthopyroxene grains display meandering texture, indicating a ductile behavior in the presence of fluid or melt- during growth of clinopyroxene grains (Fig. 3c). The Ca maps clearly show that clinopyroxene formation also occurs as veins from the fluid/melt flowing through fractures, on grain boundaries of orthopyroxene and olivine, and also as interconnected blebs and as thin bands (Fig. 3d). The meandering texture characterizing clinopyroxene-orthopyroxene boundaries (Fig. 3e, f) shows how the primary
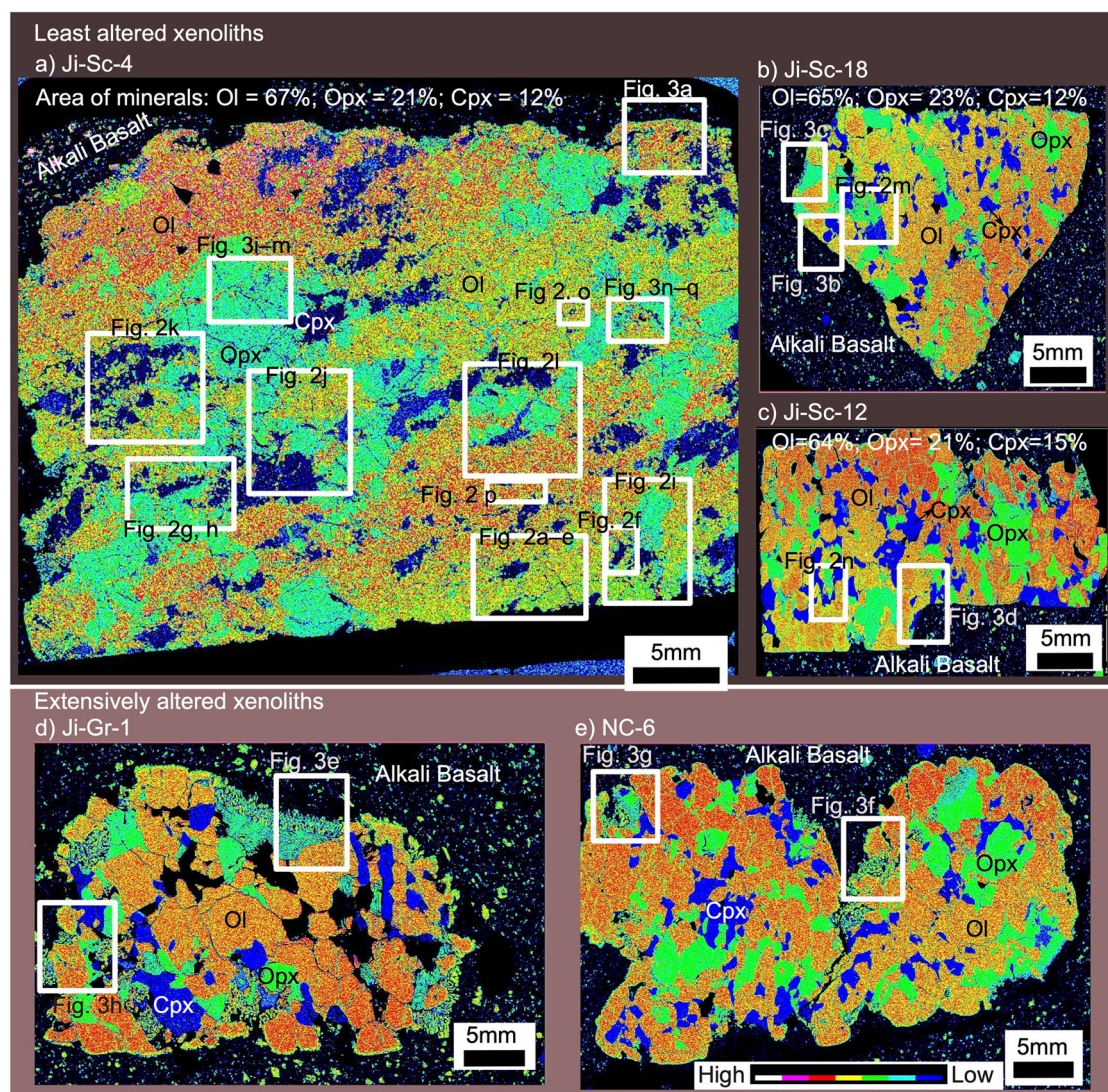
Fig. 2 Mg composition images of entire thinsection of xenoliths. a–c thinsection images of least altered group 1 xenoliths. **d, e** thinsection images of extensively altered xenoliths. Percentage of area of olivine (Ol), orthopyroxene (Opx), and clinopyroxene (Cpx) are provided at the top of images of least altered samples. Location of images used in the Figs. 2 and 3 are marked in white boxes. The color bar in panel e indicate variation in concentration of Mg from low–high in all the Mg composition maps from **a** to **e**.

fluid/melt infiltrates, dissolves the orthopyroxene grains, and forms primary clinopyroxene. Henceforth, we term this as primary melt. We also obtained enlarged elemental maps of such reactions from different areas in different samples (Fig. 3g–n). All these textural relations represent the breakdown of orthopyroxene to form primary olivine and clinopyroxene. Sporadically, minor primary spinel forms in the reaction zone (Fig. 3j, k, l). We did not observe any breakdown of original (pre-primary) olivine grains in the core of the xenoliths. Therefore, we infer that the original olivine grains might have been compositionally altered during their interaction with the infiltrated primary melt (please see details of the compositional alterations in olivine in the presence of melt in the following section). Some of the primary clinopyroxene and large spinel grains preserve relict primary orthopyroxene grains as inclusions (Fig. 3o–s).

Mineralogy and textures at rim of the least altered group 1 xenoliths: How pervasively compositional changes occur in minerals during interaction with melt/fluid is very clear at the rim of the xenoliths, where alkali basalt interacts with xenolith minerals. Primary olivine grains alter to more Fe-enriched grains (Fig. 4a) during alkali basalt interaction. Similar Fe enrichment

occurs to clinopyroxene grains (Fig. 4b, d). However, orthopyroxene broken down into new Fe-enriched olivine and clinopyroxene grains (Fig. 4c). All of these are formed during interaction with alkali basalt, which we term as secondary.

Mineralogy and textures of the extensively altered group 2 xenoliths: Breakdown of primary orthopyroxene to Fe-enriched secondary olivine and clinopyroxene occurs extensively at the xenolith core domains of the Group 2 xenoliths (Fig. 4e). This is also accompanied by complete compositional transformation of primary olivine and clinopyroxene grains into Fe-enriched secondary near at alteration sites (Fig. 4f, g). Primary spinel grains also transformed to more Fe-rich during interaction with the alkali basalt (Fig. 4h). These features also support the suggestion from previous studies[18] that the clinopyroxenitic xenoliths in this island could have originated by intense alteration of lherzolitic xenoliths by the host alkali basalt.

Variations in major element chemistry of minerals. All the spots and areas of EPMA analysis are provided in the Supplementary Fig. 5. At the core of least altered (Group 1) xenoliths,
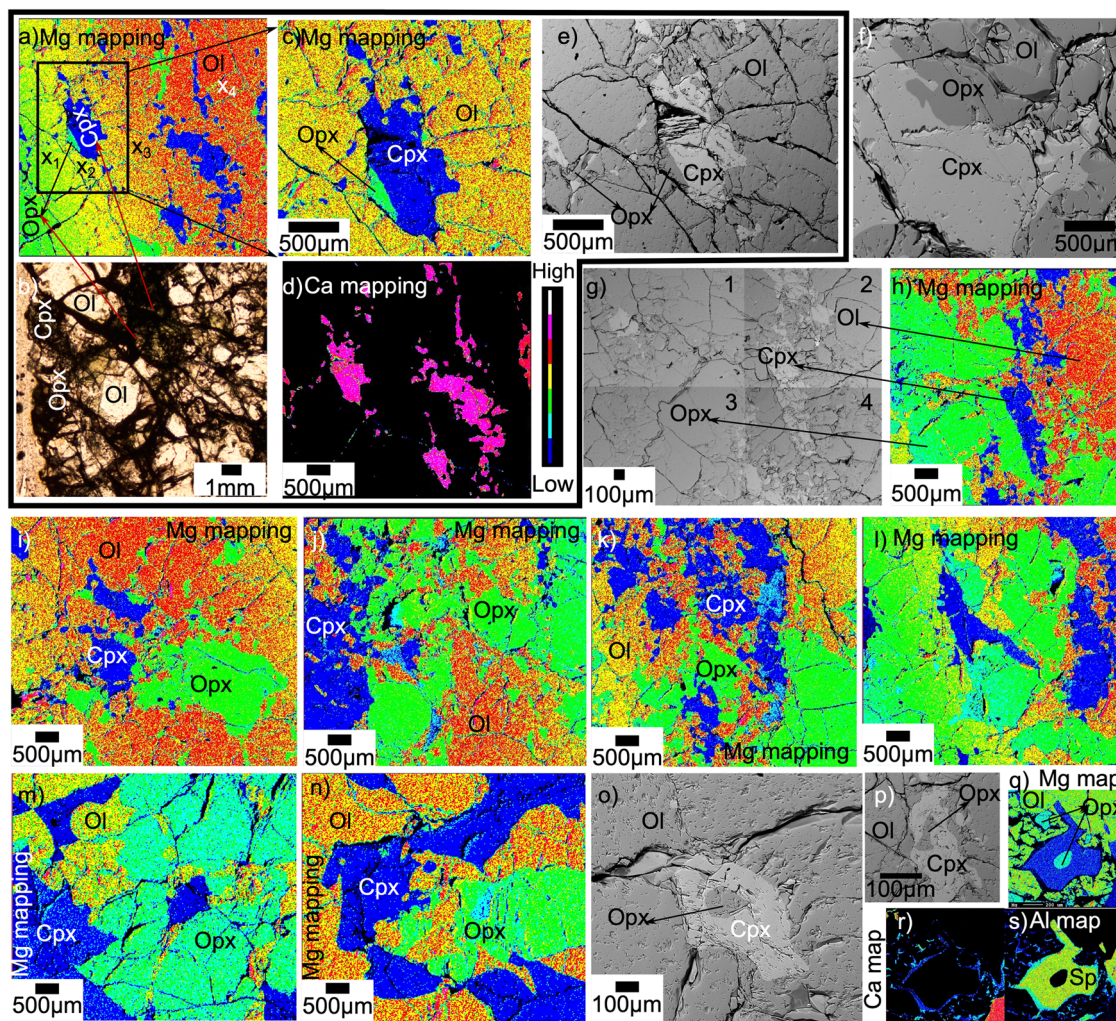
Fig. 3 Mineral replacement reactions: Core of xenoliths. a–e Images showing partial orthopyroxene replacement to olivine and clinopyroxene. **a** Residual orthopyroxene as green pockets within the reaction zone consisting of olivine and clinopyroxene grains. Olivine grains in this region show gradual change in Mg composition (X_{Mg} 0.87–0.9). **b** optical microscope image of the same area in figures **a**–**e**. **c** Magnified image of Mg map of area shows partial replacement of orthopyroxene by clinopyroxene, and meandering clinopyroxene grain boundaries indicating their melt/fluid like behavior during mineral reactions. **d** Ca map clearly shows clinopyroxene veins, blebs, and laths. **e** BSE image showing meandering grain boundaries among clinopyroxene, orthopyroxene, and olivine. **f** BSE image of meandering mineral boundaries between clinopyroxene and orthopyroxene. **g–n** Representative BSE and Mg composition images of reaction textures showing relict orthopyroxene, and formation of olivine, clinopyroxene, and spinel (1, 2, 3, 4 in image **g** are a collage of 4 BSE images). Spinel formation is minor in most samples (light blue color), (**o–s**) BSE and Mg composition images showing orthopyroxene inclusion in clinopyroxene and spinel. Ol- olivine, Opx- orthopyroxene, Cpx- Clinopyroxene, Sp- spinel. The color bar between panels **d** and **g** indicate variation in concentration of elements (Mg in **a**, **c**, **h–n**, **q**; Ca in **d** and **r**; Al in **s**) from low–high in the respective compositional maps.

major element chemistry of the primary minerals, formed by the breakdown of orthopyroxene and gradual compositional alteration of original pre-primary olivine grains, shows high-Mg composition compared to secondary olivine. Primary olivine (Supplementary Data 1) grains have forsterite composition with high variation in $X_{Mg\ (Mg/Mg+Fe)} = 0.87$–0.91. Primary orthopyroxene (Supplementary Data 2) and clinopyroxene (Supplementary Data 3) are enstatite ($X_{Mg\ (Mg/Mg+Fe)} = 0.90$–0.92) and diopside ($X_{Mg\ (Mg/Mg+Fe)} = 0.90$–0.92), respectively. Primary orthopyroxene grains have Al contents of 4–5 wt%, and primary clinopyroxene grains (precipitated from primary melt) have Al content of 5–6 wt%, respectively. An important element presented in clinopyroxene is Na. All the primary clinopyroxene grains have high Na composition of 1–2 wt%. Primary spinel (Supplementary Data 4) grains have high Mg concentration (MgO = 20–22 wt%; FeO = 10–12 wt%; Cr_2O_3 = 9–12 wt%). Compositionally, the primary pyroxenes show less variation among grains and samples

compared to large X_{Mg} variation observed in primary olivine grains, possibly indicating that olivine grains with highest Mg (0.91–0.92) content are the original (pre-primary) olivine still preserved in the samples. Most of the original olivine grains preserved in the xenoliths could be compositionally altered to primary olivine composition during primary melt interaction. Therefore, percentage of original olivine compared to primary olivine is very low. We could rarely identify such original olivine with $X_{Mg} > 90$. All the clinopyroxene grains are identified as primary (no presence of any pre-primary clinopyroxene) based on their high-Na content.

At the rim of the least altered (Group 1) xenoliths, interaction with the host basalt generated the secondary olivine composition on rims of primary grains with less X_{Mg} of 0.86–0.61 (Supplementary Data 1), which is formed by breakdown of orthopyroxene and gradual compositional alteration of primary olivine grains. Interaction with host basalt also generated
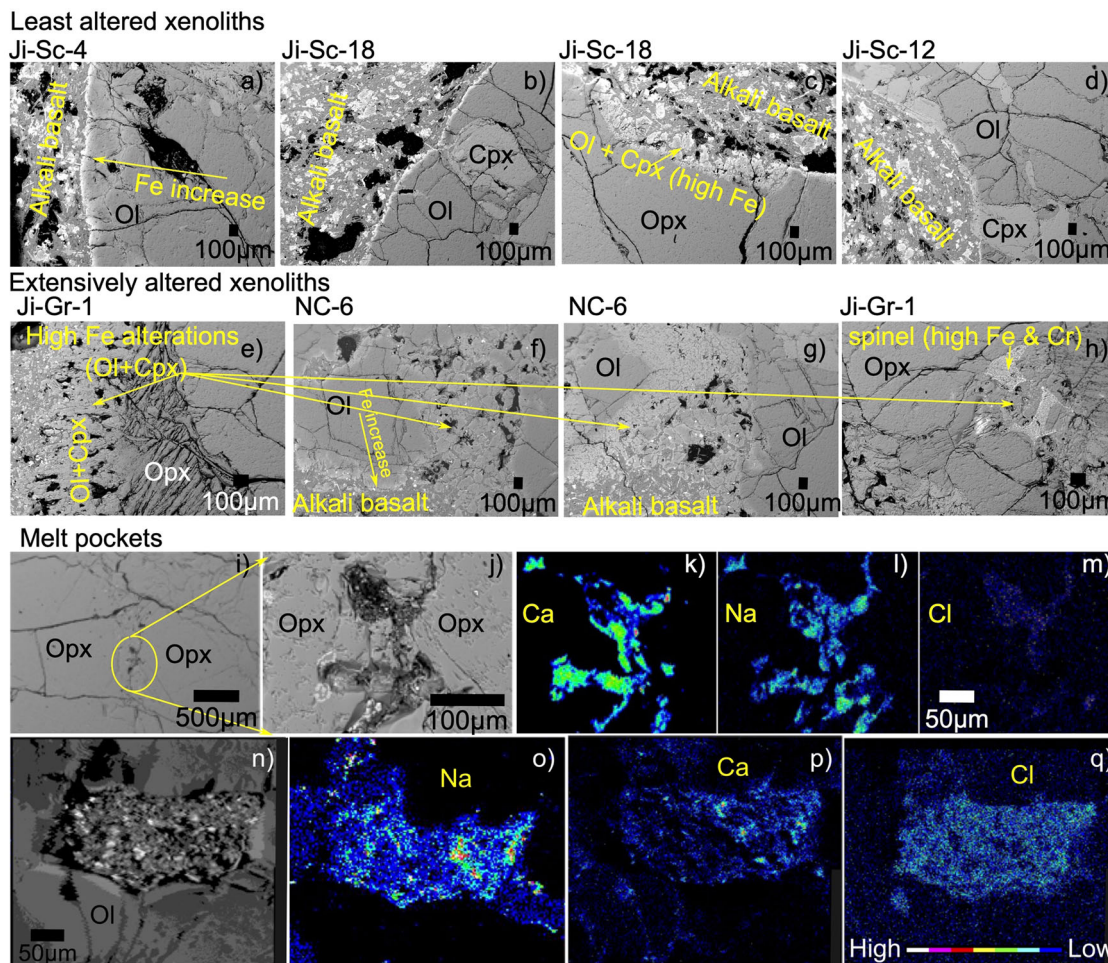
Fig. 4 Characteristics of xenolith-alkali basalt interactions, and melt pockets at the core of least altered xenoliths. a–d Xenolith-alkali basalt interaction at the rim of Group 1 least altered xenolith samples. Less than 1 mm of xenolith boundary is affected by the interaction. Fe concentration gradually increase in the olivine and clinopyroxene grains near the rim. Orthopyroxene breaks down to Fe rich olivine and clinopyroxene. **e–h** Xenolith-alkali basalt interaction in the Group 2 extensively altered xenolith samples. Extensive breakdown of orthopyroxene grains to olivine and clinopyroxene occurs within the core of xenoliths. Primary olivine, clinopyroxene, and spinel alters to secondary Fe rich composition within the xenolith. **i–q** BSE and Ca, Na, Cl composition images of melt pockets in Group 1 least altered sample (Ji-Sc-4). Ca, Na, and Cl enrichment in these pockets may be indicate characteristics of primary melt. Abbreviations: Ol- olivine, Opx- orthopyroxene, Cpx- Clinopyroxene, Sp- spinel. The color bar in panel **q** indicate variation in concentration of elements (Ca, Na, Cl in **k–m**, **o–q**) from low–high in the respective compositional maps.

secondary clinopyroxene grains, formed by the breakdown of orthopyroxene and the gradual compositional alteration of primary clinopyroxene grains, with $X_{Mg} = 0.88$–0.7, and have low Na composition (0.2–0.5 wt%) (Supplementary Data 3). Spinel grains altered by the host basalt have Fe and Cr enrichments (MgO = 16–19 wt%; FeO = 12–16 wt%; $Cr_2O_3 = 12$–15 wt%) on their rims compared to the primary spinel (Supplementary Data 4).
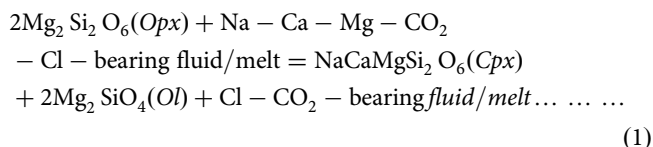
Extensively altered (Group 2) xenoliths: These samples still preserve some portions of primary compositions similar to the core of the least altered xenoliths (Supplementary Data 1, 3, and 4). The secondary minerals formed at the alteration zones also show similar compositional variations as rim of the least altered xenoliths (Supplementary Data 1, 3, and 4). However, the extent of alteration is large compared to the least altered samples, and formed alteration pockets within the xenolith core (Figs. 2d, e and 4 e-h).

Composition and implications of melt pockets in the core of the Group 1 xenoliths: Our textural observations from the cores of Group 1 xenoliths provide important and direct evidence of orthopyroxene breakdown reactions. Except for Ca, all other elements were possibly provided by the breakdown of orthopyroxene. Meandering textures of clinopyroxene at the reaction zone clearly indicate infiltration of externally-derived Ca dissolved in fluid/melt. Previous studies have confirmed high CO_2 concentration in fluid inclusions in the xenolith samples from this island[26]. However, in our study, we observed Cl-enriched melt pockets (Fig. 4 i–q) that were qualitatively analyzed using 15 μm beam diameter to show their approximate composition. Separate analysis of different phases is difficult due to the intermingling of minute irregular grains and narrow melt channels. Melt pockets in the Group 1 xenolith (sample no. Ji-Sc-4) shows high Na ($Na_2O \sim 8$ wt%) and Cl (2–6 wt%) compositions (Supplementary Table 2). Such melt pockets enriched in Ca, Na, Cl along with Mg, Fe, Ni, S, and Si (Supplementary Table 2) may represent primary melt enriched in Na- Ca- Cl- CO_2- with dissolved components (Mg, Fe, Si etc) in them.

Further studies on the melt pockets and clinopyroxene separates could provide more details of the processes that generate the Na- Ca- Cl- CO_2- enriched melt in the deeper mantle. Based on the above observations, the orthopyroxene breakdown reaction to form primary olivine and clinopyroxene

(high Na could be represented by Eq. (1)).

$$
\begin{aligned}
2Mg_2\,Si_2\,O_6(Opx) &+ Na - Ca - Mg - CO_2 \\
&- Cl - bearing\ fluid/melt = NaCaMgSi_2\,O_6(Cpx) \\
&+ 2Mg_2\,SiO_4(Ol) + Cl - CO_2 - bearing\ fluid/melt\ldots\ldots\ldots
\end{aligned}
$$
(1)

Variations in trace element chemistry of minerals. All the spots of LA-ICPMS analyses are shown in Supplementary Fig. 6. Our data show that clinopyroxene grains are comparatively enriched in most of the trace elements and rare earth elements (REE's) compared to orthopyroxene (enriched in few HREE's) and olivine (enriched in Ni, Mn etc (Fig. 5a, b, Supplementary Fig. 7a, b, and Supplementary Data 1 and 5–7). Primary and secondary clinopyroxene grains show different patterns in chondrite[27]-normalized REE concentration (Fig. 5a, b, d). The REEs of primary clinopyroxene grains show a spoon-shaped pattern (Fig. 5a). This REE pattern is characteristic, of the chromatographic effects of the infiltrating fluid/melt[28,29], in this case Na- Ca- Cl- CO$_2$- enriched fluid/melt. During this infiltration process, the enrichment front of the most incompatible elements (La, Ce etc.) infiltrates faster through the rock compared to the less incompatible ones[28,29]. Secondary clinopyroxenes, formed due to interaction with host basalt, are enriched in LREE's compared to primary clinopyroxenes (Fig. 5b–e). The host basalt has high LREE and relatively low abundance of HREE's (black line in Fig. 5c). Primary clinopyroxene grains, next to secondary clinopyroxene (formed by interaction with alkali baslat), shows a LREE depleted pattern instead of a spoon-shaped pattern (Fig. 5d, e). This possibly indicates that most incompatible elements like La, Ce etc. diffused from the primary clinopyroxene to the secondary clinopyroxene near alkali basalt infiltration sites.

The Na- Ca- Cl- CO$_2$-enriched primary fluids/melts could have generated the spoon-shaped REE concentration, while infiltering through the asthenosphere and before interacting with upper mantle lherzolites. In addition to this, trace elements indicating any subduction influence[30] (LREE's, Rb, Ba, Nb, Pb, Sr etc.) are absent or present in very low concentration (<10 ppm) in primary clinopyroxene grains (Supplementary Fig. 7a and Supplementary Data 5–7) Primitive mantle normalized[27] compositions show enrichment of HREE's in primary and seconday clinopyroxene grains and are similar to the enrichment-depletion pattern of orthopyroxene grains (Supplementary Fig. 7a–c and Supplementary Data 5 and 7). This is another evidence for the dissolution of orthopyroxene grains during the formation of clinopyroxene grains (as we see in their textural relationship). We have calculated the equilibrium melt composition from primary and secondary clinopyroxene composition using published partition coefficients[31–33] (Supplementary Fig. 7c, Supplementary Data 7). Primitive mantle normalized[27] values of equilibrium melt calculated from primary clinopyroxene data are comparatively depleted than those of equilibrium melt calculated from secondary clinopyroxene data (Supplementary Fig. 7c). Prominent depletion of Zr, Hf of equilibrium melt calculated from primary clinopyroxene data follow the pattern of a Cl-rich kimberlite[34] melt compared to composition of carbonatite melt[35] and alkali basalt from Jeju island[36] (Supplementary Fig. 7c and Supplementary Data 7). Secondary clinopyroxene grains, compared to primary clinopyroxene, have a higher concentration of elements (such as LREE's, Rb, Ba, Nb, Pb, Sr etc.) and depletion in Y and HREE's indicating a subduction influence[30] (Supplementary Fig. 7a and Supplementary Data 6 and 7). Further the equilibrium melt calculated from secondary clinopyroxene shows trends (e.g. enriched Zr-Hf) similar to carbonatite melt[35] and

alkali basalt from Jeju Island[36]. Therefore, subducted oceanic crust (eclogite) with carbonate minerals may be components in the source of alkali basalt melt[37,38].

Olivine grains are enriched in trace elements like Ni and Mn (Supplementary Data 1). They show a marked variation in the ratio of NiO and MnO with respect to original (pre-primary), primary (formed from orthopyroxene), and secondary (formed due to interaction with host alkali basalt) compositions (Fig. 5f, Supplementary Data 1). Original olivine grains, with highest Mg# (>0.90) possibly derived from melt extraction events in the Archean, have the highest NiO/MnO value of ~3.5. Primary olivine grains produced due to orthopyroxene breakdown show a range in NiO/MnO values from 3.5 to 2. Previous experimental studies[39] on the partitioning of Ni, Mn in olivine phenocrysts in basalts suggests that their ratio could be correlated to the depth of lithosphere-asthenosphere boundary from where the basaltic/komatiitic partial melts are extracted from peridotite. If we assume batch melting of peridotite, the residue of such melt would be in equilibrium with respect to the Ni/Mn ratio in basaltic olivine. Therefore, it is logical to correlate Ni/Mn ratio in residual peridotite olivine to the depth of the lithosphere-asthenosphere boundary inferred from olivine grains in basalt/komatiite. Such correlations suggest that original olivine compositions in these xenoliths could have originated when the lithosphere-asthenosphere boundary was at a depth of 60–100 km (2–3 GPa). This ratio shows a slight variation from 3.5 to 2 in new olivine grains formed by primary melt interaction. Since Mn partitioning strongly depends on pressure and bulk Mg#[39], and Ni partitioning depend on temperature[39], we could assume (if the system is closed for Ni and Mn) that new olivine grains with NiO/MnO ratio of 3.5 indicate that lherzolite formation was initiated at a depth of 60–100 km. Further infiltration of fluids and cooling could have reduced the NiO/MnO ratios to 2 in primary olivine grains. Subsequent interaction of these xenoliths with alkali basalt, enriched in Mn, could have lowered the ratio of Ni and Mn in olivine grains with low Mg# (<87). The ratio of Ni and Mn with respect to Mg# provide a trend of geochemical alteration observed in the xenoliths (Fig. 5f).

Oxygen isotope variations in minerals. All the spots of Secondary-Ion Mass Spectrometry (SIMS) analyses are provided in the Supplementary Fig. 8. Estimates of $\partial^{18}O$ of Bulk Silicate Earth (primary mantle source), and measurements $\partial^{18}O$ of meteorites, moon samples, mantle peridotites range from 5.1 to 5.9‰[40–42]. The oxygen isotope ratio of primary olivine, orthopyroxene, and spinel in the Group 1 (least altered samples) fall within this range (Fig. 5g (Ol- 1, 2; Opx- 1, 2; Sp-1); Supplementary Table 3). The oxygen isotope ratio ($\partial^{18}O$) of rocks are very sensitive to the $\partial^{18}O$ of infiltrating fluid or melt[40–42]. Since these are fertile lherzolite xenoliths that show the infiltration of primary melt, the ratios in primary minerals are comparable to the $\partial^{18}O$ of this melt. This suggests that Na- Ca- Cl- CO$_2$-enriched (may be parental kimberlite) melt, that altered the original harzburgites, might have originated in the deeper mantle. The Group 2 samples, which were extensively altered by the host alkali basalt, show high values of $\partial^{18}O$ of 2–4 ‰ increase (Fig. 5g (Ol- 3; Opx- 3); Supplementary Table 3). A similar high oxygen isotopic composition is also reported from the alkali basalts generated during the Late Cenozoic in various part of East Asia, for example 24 to 0.3 Ma (Late Cenozoic) alkali basalts in Shandong Province, eastern China show high values of $\partial^{18}O$ of 6–8.4 ‰[43]. Such high values suggest the role of the recycled subducted oceanic slab components (e.g., eclogite + marine sediments) in the generation of alkali basaltic magma[43–46].
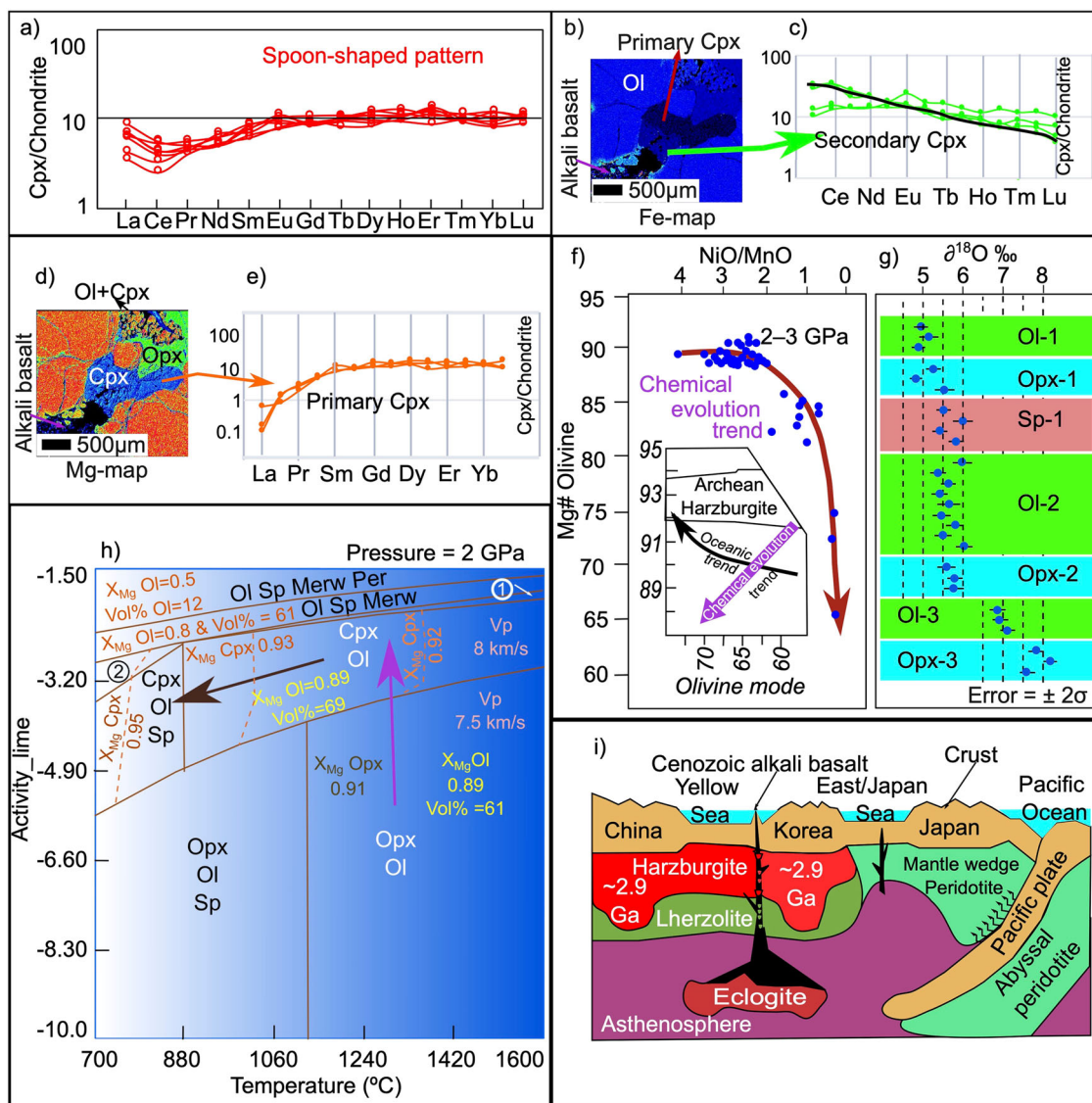
Fig. 5 Trace elements, Oxygen isotope, Pseudosection, and Schematic image of East Asian lithosphere. a Spoon shaped chondrite normalized[27] Rare Earth Elements (REE) pattern of primary clinopyroxene grains (Supplementary Data 5). **b** Fe composition map of xenolith-alkali basalt interaction site. Gradual Fe enrichment altering primary clinopyroxene to secondary is visible at the center of the image. **c** secondary (Fe rich) clinopyroxene showing chondrite normalized[27] LREE enrichment (Supplementary Data 5). Black line shows chondrite normalized[27] average REE pattern of alkali basalt (Supplementary Data 5). **d** Mg composition map of xenolith-alkali basalt interaction site shown in figure **b**. **e** Chondrite normalized[27] REE pattern of primary clinopyroxene near the secondary clinopyroxene showing LREE depletion (Supplementary Data 5). **f** a curved red arrow showing the variation of ratio of NiO and MnO with respect to Mg# (100x Mg/(Mg+Fe-total)) (Supplementary Data 1). Picture in the inset is showing schematic representation of opposite trends of the evolution of depleted peridotites of oceanic lithosphere (oceanic trend[10] (black arrow)) and the chemical evolution (purple arrow) of continental lherzolites (in this study) with respect to the Mg # of depleted Archean harzburgites[10]. Please see the explanation of values used in this inset figure in the 'chemical evolution trend of peridotites in the continental lithospheric mantle section'. **g** Variation in the oxygen isotope composition ($\partial^{18}O$-per mil (‰)) of Group 1- least altered by alkali basalt (sample no. Ji-Sc-4 (Ol-1, Opx-1, Sp-1), and Ji-Sc-18 (Ol-2, Opx-2)), and Group 2- intensely altered by alkali basalt (sample no. NC-6 (Ol-3, Opx-3)). Error bars are ± 2 sigma (SD) (Supplementary Table 3). **h** Pseudosection showing transformation of harzburgite to lherzolite with respect to increasing lime activity (purple arrow). Clinopyroxene with maximum $X_{Mg} = 0.92$ is stable at temperature ~1200–1400 °C, lime activity of 10^{-3} to 10^{-4}, and at a pressure of 2 GPa. Spinel formation occurs during the cooling stage (brown arrow). The harzburgite to lherzolite mineralogical transformation is also characterized by change in volume % of olivine from 61 to 69, and an increase in seismic primary wave velocity from 7.5 km/s to 8 km/s. The circle 1 in the figure has phases- Ol, Cpx, Merw, and 2 has - Ol, Cpx, Sp. Ol- olivine, Opx- orthopyroxene, Cpx- Clinopyroxene, Sp- spinel, Merw-merwinite. **i** A cartoon depicting lithosphere-asthenosphere interactions beneath East-Asian countries. Both Korea and China consist of a thick lithospheric mantle (consisting of Archean harzburgite (2.9 Ga) partially altered to lherzolite during Paleozoic kimberlite volcanism) compared to Jurassic mantle wedge beneath Japan. The Pacific subduction zone could have introduced crustal lithologies (e.g. carbonated eclogite + sediments) to the asthenospheric mantle and might be the source of Cenozoic alkali basalt volcanism in the East Asian continents.

Pseudosection modeling. We performed pseudosection modeling (details given in the Methods section) to understand the evolution of primary mineral assemblages during the harzburgite to lherzolite transformation (Fig. 5h). Pressure and temperature conditions of primary melt interaction is calculated using geothermo-barometer based on clinopyroxene chemistry only[47,48] (This geothermobarometer (MagMin_PT) is based on traditional computations, and machine learning methods[49]).

These results indicate a pressure of ~2 GPa and temperature of ~1300 °C (Supplementary Data 3). The Ni/Mn ratio of primary olivine grains show similar depths for these samples as well as pressure estimations in previous studies using the xenolith samples[18,50]. Lherzolite composition has a high- Ca activity due to Ca rich externally-derived chloride-carbonatite fluids/melt infiltration. Clinopyroxene-olivine assemblage with maximum X_{Mg} (Cpx) of 0.92 occurs at ~log lime activity of −3 to −4 and at temperature ~1250–1400 °C. At this condition, olivine has X_{Mg} of 0.89. Further at low Ca activity, the orthopyroxene ($X_{Mg} = 0.91$)-olivine ($X_{Mg} = 0.89$) assemblage is stable, representing the mineralogy of harzburgite xenoliths. Olivine grains with highest Mg# of 92 is typical of the high degree of melting in the Archean[4,5]; this is not reproduced in our pseudosection calculations, since the processes leading to the formation of residual harzburgite with high Mg olivine in the Archean is largely uncertain, and are not verified by experiments or included in the modeling programs. Spinel formation mostly occurs when the rock cools to a lower temperature of ~900 °C. The close association of spinel with pyroxenes suggests that Al for the spinel formation could have been supplied by pyroxenes.

Chemical evolution trend of peridotites in the continental lithospheric mantle. Our textural observations suggest that orthopyroxene interaction with both primary melt (kimberlitic) and secondary melt (alkali basalt) generated additional olivine in the peridotite. During these interactions, Fe content of pre-existing olivine also increased. There is no textural evidence of olivine dissolution in these samples. This suggests an increase in the modal olivine percentage (volume %) increased during chemical alteration of peridotites by both melts. This observation is also supported by our pseudosection model. Modal olivine percentage increases during increase in Ca activity. This value ranges from 61 to 69. Modal olivine percentage calculated directly in our least altered samples (that are affected by primary melt) are 64–67 with respect to minimum olivine Mg#87. All these observations and data allowed us to interpret that the modal percentage (volume %) of olivine increases from 61 to 69 with respect to a decrease in Mg# to 87 from an original value of 92 of Archean depleted harzburgite (inset in Fig. 5f). Variation in Mg# of olivine with respect to modal olivine percentage defines an oceanic trend of Proterozoic and Phanerozoic upper mantle depleted peridotites compared to Archean depleted counterparts[4,10] (inset in Fig. 5f). In the modern abyssal depleted peridotites Mg# of olivine shows an increase to 92 as the modal olivine percentage increases[4,10]. However, in the present case of the formation of fertile lherzolite from depleted harzburgites in continental roots, there is a decrease in Mg# with respect to increase in modal olivine percentage. We define this as a trend of chemical evolution of depleted to fertile peridotite in the upper mantle beneath the continents (inset in Fig. 5f). Such mineralogical changes also accompany an increase in the P-wave velocity of seismic waves from 7.5 km/s to 8 km/s as we move from harzburgite to lherzolite in composition (Fig. 5h). Previous seismic studies have attributed a high velocity for depleted harzburgite and a low velocity for intrusion of the asthenosphere within the lithospheric mantle[51]. On the contrary, our study suggests that mineralogical changes during chemical evolution of upper mantle could increase the P-wave velocity compared to depleted peridotite roots (Fig. 5h).

Discussion

Orthopyroxene replacement textures, and mineral chemistry data (major, trace, and ∂18O) in younger lherzolite xenoliths provide direct evidence of geochemical evolution of highly depleted harzburgitic to fertile lherzolitic transformation of the upper mantle, rather than wholescale delamination of Archean peridotites in the continental roots and substitution of new mantle roots. The Rhenium (Re) depletion model ages (T_{RD}) of extremely melt-depleted (partial melting of ~30%) continental peridotite xenoliths constrain the true melt depletion age, assuming complete removal of incompatible Re compared to Os during extreme melting events[52,53]. In east Asia, the harzburgitic xenoliths shows older melt depletion ages of ca. 2.5–2.9 Ga in the North China Craton and ca. 1.8–1.9 Ga in the South Korean Peninsula[14,19]. However, high uncertainties are expected in dispersed younger T_{RD} values (1.8–0.13 Ga in the North China Craton, 1.1–0.15 Ga in the South Korean Peninsula) of lherzolite xenoliths due to more recent melt metasomatism[52–54]. Therefore these younger ages cannot be correlated to any true geological events.

We identified two episodes of geochemical alteration of depleted harzbugitic upper mantle roots based on our data from the Jeju Island. First, during its interaction with primary melt enriched in Na- Ca- Cl- CO₂, and second during its interaction with an alkali basalt melt. A recent experimental study suggests that a large amount of Cl might be transported to the mantle via deep subduction[55]. Chlorine-rich kimberlites of the Udachnaya-East Pipe, Yakutia, Russia[34,56] also support such experimental results. Based on our textural and geochemical results, we hypothesize that interaction of the primary melt enriched in Na-Ca- Cl- CO₂- with peridotite dissolves silicate components of peridotite, and possibly generate a parental kimberlitic melt. Such kimberlitic pipes carrying depleted Archean harzburgites and garnet lherzolites are present in both the North and South China Cratons in East Asia[14,57]. Therefore, it is reasonable to consider that Paleozoic kimberlitic magmatism in East Asia could have partially altered the depleted harzburgitic roots to fertile lherzolitic in composition. Since no major tectonic event coincide with such kimberlitic magmatism, we suggest that mantle plumes could be the trigger for the first-generation melt metasomatism in the Paleozoic in East Asia. The second alteration caused by alkali basalt has enriched Fe, REE's, ∂18O, and subduction-derived trace elements on secondary minerals. This suggests that the remnants of carbonated subducted slab (with sediments) have a major influence in generating alkali basalt magma[37,38] (Fig. 5i). Examples of immediate association of alkali basalt and carbonated silicate melts, and experimental studies on carbonated eclogites suggest that such an alkali basalt melt could have formed from the asthenosphere bearing carbonated eclogitic residues[37,38]. The low viscosity of carbonated silicate melt/carbonatite could have reactively percolated through the thick lithosphere and evolved to alkali basalt magma[37,38]. Since harzburgitic roots were partially altered to lherzolite during the kimberlitic melt interaction in the Paleozoic, Cenozoic alkali basalt volcanism in the entire region carry mostly lherzolite xenoliths with minor harzburgite xenoliths (Fig. 5i).

A transition from highly depleted harzburgite to fertile lherzolite xenoliths is not only observed in East Asia but is also a characteristic of Archean and Proterozoic terranes worldwide[12,13]. Our study suggests that such Fe- enriched (low Mg# of olivine) fertile peridotites could have been generated by the interaction of depleted peridotite with kimberlitic (Mg# of olivine ~87–91) or alkali basalt (Mg# of olivine <87) melt. Therefore, our results are in general indicate how mineralogical and geochemical variations observed in depleted and fertile continental xenoliths present worldwide might indicate the geochemical evolution of the upper mantle throughout Earth's history.

Conclusions

The direct evidence of mantle replacement reactions presented in our study indicates that root/keel of continents are very stable (i.e., resistant to recycling). Since both kimberlitic and alkali basaltic magmas sample the deeper portions of continental roots, presence of harzburgitic xenoliths in the recent volcanic eruptions indicates that the Archean roots of continents were preserved at the lithosphere-asthenosphere boundary. This suggests that the last ca. 2.5 Ga of mantle processes could only alter small proportions of lower portions of the continental roots. Stability of upper mantle roots of continents indicate that oceanic lithosphere (without any contribution of continental lithosphere) is the only component mixing in the deeper mantle since the Archean. This suggests that the deeper mantle geochemically evolves during mid-ocean ridge partial melting events and oceanic lithosphere return via subduction. Such cyclic events could have recycled most of the mantle through mid-ocean ridges at least once[58,59]. However, many studies predicted that large scale mechanical homogenization of the whole mantle on geologic timescales is difficult[58–60]. Therefore, the deeper mantle could be a mechanical mixture of subducted chemically altered oceanic lithosphere and refractory peridotite of mid-ocean ridge melting, attesting to a two-component marble-cake model[58]. Our results suggest long term stability of continental lithosphere, and two component evolution of Earths' deeper mantle through time.

Methods

Electron Probe Micro Analyzer analysis. Composition of minerals in lherzolite samples were determined by a 5 channel - JEOL JXA-8100 Superprobe, Electron Probe Micro Analyzer (EPMA), housed at the Department of Earth System Sciences, Yonsei University, Seoul, South Korea. Analytical conditions are accelerating voltage of 20 kV; beam current of 20 nA; counting time of 10 s; an electron beam spot size of 15 μm. Due to their volatile nature, Na, K were kept first in the analysis list for the analysis of minerals. Natural and synthetic silicates and oxides supplied by JEOL and ASTIMEX Standards Ltd., Canada, were used for calibration of oxides of all major elements. Relative errors in EMPA are estimated to be <1% at the >10 wt% level, 5–10% at the 1–10wt % level, 10–20% at the 0.2 to 1wt % level, and 20–40% at the < 0.1wt % level. The data were reduced using the ZAF correction procedures supplied by JEOL.

Pseudosection modeling. Pseudosection was computed for the lherzolite bulk composition using the hp02ver.dat database implemented in the Perple_X (version 6.7.9) software[61]. The bulk chemistry[18] of lherzolite sample is $SiO_2 = 45.29$, $Al_2O_3 = 2.74$, $MgO = 41.68$, $FeO = 9.36$. The components such as TiO_2, P_2O_5, Na_2O, K_2O, and MnO have been removed from the bulk chemistry because of its absence or low concentration (<0.1 wt%) in the whole rock chemistry. CaO has been treated as an independent component and its activity is varied from 10^{-1} to 10^{-10}. The mineral solid solution models for following minerals clinopyroxene; orthopyroxene, olivine and spinel were selected for the calculation[62,63]. The two-dimensional pseudosection was calculated, where temperature changes from 700 to 1600 °C on the X-axis and log activity lime varies from −1 to −10 on the Y-axis at a constant pressure of 2 GPa.

Laser Ablation Inductively Coupled Plasma Mass Spectrometry analysis. In situ analysis of trace elements in olivine, clinopyroxene, and orthopyroxene in lherzolite samples were conducted at Korean Basic Science Institute (KBSI), South Korea using 193 nm ArF Excimer Laser Ablation Inductively Coupled Plasma Mass Spectrometry (Teledyne Cetac Technologies equipped with Analyte Excite). Analytical conditions are spot size: 50 μm, laser repetition rate: 10 Hz, energy density: 5 J/cm2 per pulse, and a dwell time: 20 s. Calibration was achieved using the NIST SRM 612 glass with the reference values[64] and was analyzed after every 5 analysis of minerals. Accuracy of data is also double checked with olivine, orthopyroxene and clinopyroxene samples with known composition. Each analysis was normalized using[29] Si as internal standard, based on Si contents obtained by electron probe micro analysis (EMPA). We have analyzed clear homogenous areas of minerals and each mineral was analyzed at least three times. Data reduction was done by using Glitter software, developed by the ARC National Key Centre for Geochemical Evolution and Metallogeny of Continents (GEMOC) and CSIRO Exploration and Mining. The relative standard deviations (RSD) of the trace and rare earth elements in the minerals were mostly 5–10%.

Secondary-Ion Mass Spectrometry analysis. Oxygen isotopes composition of olivine, orthopyroxene and spinel were measured using a Cameca IMS1300-HR3 large-geometry SIMS at the *Korean Basic Science Institute (KBSI), South Korea*. The sample mount was gold coated (20 nm) for analysis. A spot size of ~15 μm on the mineral surface was ablated by focused Cs+ primary ion beam (Gaussian mode) accelerated at 10 kV and ~3.0 nA ion current. Secondary ions generated from the mineral were accelerated to (−10 kV) field aperture set at a magnification of ~200 to allow maximum secondary ion transmission. Instrument settings were contrast aperture: 400 μm diameter, entrance slit: ~70.3 μm width, field aperture: 3000×3000 μm², and energy slit: 50 eV width at the low- energy peak. Oxygen isotope ions ($^{16}O-$ and $^{18}O-$) were detected simultaneously using two Faraday cups with 1010 Ω ($^{16}O-$) and 1011 Ω ($^{18}O-$) pre-amplifiers. A 500-μm exit slit with a mass-resolving power of ~ 2000 was used for both detectors and noticed count rates of ~3×109 cps ($^{16}O-$) and ~6×106 cps ($^{18}O-$). The internal precision of $^{18}O/^{16}O$ measurement was ~0.2‰ (20 cycles, 2 standard errors). Olivine, orthopyroxene and spinel grains with known oxygen isotope compositions were used to calibrate the data. These standard grains were measured before and after three analysis of each mineral grain.

Data availability

All data used in this manuscript including sample locations, EPMA data, LA-ICPMS data, and SIMS data are provided in Supplementary Tables 1–3 and Supplementary Data 1–7. These datasets are also available in the Figshare repository https://doi.org/10.6084/m9.figshare.24549832.

References

1. Moore, W. B. & Lenardic, A. The efficiency of plate tectonics and nonequilibrium dynamical evolution of planetary mantles. *Geophys. Res. Lett.* **42**, 9255–9260 (2015).
2. Windley, B. F. *The Evolving Continents* (John Wiley and Sons, 1984).
3. Condie, K. C. *Plate Tectonics And Crustal Evolution* (Pergamon, 1989).
4. Boyd, F. R. The origin of cratonic peridotites: a major-element approach. *Int. Geol. Rev.* **40**, 755–764 (1998).
5. Servali, A. & Korenaga, J. Oceanic origin of continental mantle lithosphere. *Geology* **46**, 1047–1050 (2018).
6. Boyd, F. R. & Mertzman, S. A. *Magmatic Processes: Physicochemical Principles* (ed. Mysen, B. O.) 13–24. Spec. Publ. Vol. 1, (Geochemical Society, University Park, 1987).
7. Boyd, F. R. et al. Composition of the Siberian cratonic mantle: evidence from Udachnaya peridotite xenoliths. *Contrib. Mineral. Petrol.* **128**, 228–246 (1997).

8. Menzies, M. A., Fan, W.-M. & Zhang, M. *Magmatic Processes and Plate Tectonics* (eds. Prichard, H. M., Alabaster, T., Harris, N. B. W. & Neary, C. R.) 71–81. Vol. 76, (Geological Society, 1993).

9. Griffin, W. L., Zhang, A. D., O'Reilly, S. Y. & Ryan, C. G. *Mantle Dynamics and Plate Interactions in East Asia* (eds. Flower, M. Chung, S.-L., Lo, C.-H. & Lee, T.-Y.) 107–126 (American Geophysical Union, 1998).

10. Boyd, F. R. Compositional distinction between oceanic and cratonic lithosphere. *Earth Planet. Sci. Lett.* **96**, 15–26 (1989).

11. Lee, C. T. et al. Preservation of ancient and fertile lithospheric mantle beneath the southwestern United States. *Nature* **411**, 69–73 (2001).

12. Carlson, R. W., Pearson, D. G. & James, D. E. Physical, chemical, and chronological characteristics of continental mantle. *Rev. Geophys.* **43**, RG1001 (2005).

13. O'Reilly, S. Y., Griffin, W. L., Poudjom Djomani, Y. H. & Morgan, O. Are lithospheres are forever? Tracking changes in sub- continental lithospheric mantle through time. *GSA Today* **11**, 4–10 (2001).

14. Gao, S., Rudnick, R. L., Carlson, R. W., McDonough, W. F. & Liu, Y.-S. Re–Os evidence for replacement of ancient mantle lithosphere beneath the North China Craton. *Earth Planet. Sci. Lett.* **198**, 307–322 (2002).

15. Lee, C.-T., Yin, Q.-Z., Rudnick, R. L., Chesley, J. T. & Jacobsen, S. B. Osmium isotopic evidence for Mesozoic removal of lithospheric mantle beneath the Sierra Nevada. *Science* **289**, 1912–1916 (2001).

16. Bird, P. Continental delamination and the Colorado Plateau. *J. Geophys. Res.* **84**, 7561–7571 (1979).

17. Bajolet, F. et. Continental delamination: insights from laboratory models. *Geochem. Geophys. Geosyst.* **13**, Q02009 (2012).

18. Choi, S. H., Kwon, S.-T., Mukasa, S. B. & Sagong, H. Sr–Nd–Pb isotope and trace element systematics of mantle xenoliths from Late Cenozoic alkaline lavas, South Korea. *Chem. Geol.* **221**, 40–64 (2005).

19. Lee, S. R. & Walker, R. J. Re–Os isotope systematics of mantle xenoliths from South Korea: Evidence for complex growth and loss of lithospheric mantle beneath East Asia. *Chem. Geol.* **231**, 90–101 (2006).

20. Kim, S. W. et al. Tracking Paleozoic evolution of the South Korean Peninsula from detrital zircon records: implications for the tectonic history of East Asia. *Gondwana Res.* **50**, 195–215 (2017).

21. Kim, S. W. et al. Detrital zircon U-Pb and Hf isotope characteristics of the Early Neoproterozoic successions in the central-western Korean Peninsula: Implication for the Precambrian tectonic history of East Asia. *Precambrian Res.* **322**, 24–41 (2019).

22. Lee, M. W. Petrology and geochemistry of Jeju volcanic island, Korea. *Tohoku Univ. Sci. Rep. Ser.* **3**, 177–256 (1982).

23. Won, C. K., Matsuda, J., Nagao, K., Kim, K. H. & Lee, M. W. Paleomagnetism and radiometric age of trachytes in Jeju Island. *J. Korean Inst. Mining Geol.* **19**, 25–33 (1986).

24. Yun S. K., Han D. S. & Lee D. Y. *Quaternary geology in the Southern part of Jeju Island*. Report KR-86–2 (B)-2, (Korea Institute of Geology, Mining and Material, 1986).

25. Lee D. Y., Yun, S. K., Kim, J. Y. & Kim, Y. J. *Quaternary Geological Survey of Cheju Island*. Report KR-87–29, (Korea Institute of Geology, Mining and Material, 1987).

26. Seo, M. et al. Mantle-derived CO_2-fluid inclusions in peridotite xenoliths from the Alkali Basalt, Jeju Island, South Korea. *J. Petrol. Soc. Korea* **25**, 39–50 (2016).

27. Sun, S.-S. & McDonough, W. F. Chemical and isotopic systematics of oceanic basalts: implications for mantle composition and processes. *Geol. Soc. Spec. Publ.* **42**, 313–345 (1989).

28. Navon, O. & Stolper, E. Geochemical consequence of melt percolation: the upper mantle as a chromatographic column. *J. Geol.* **95**, 285–307 (1987).

29. Bodinier, J. L., Vasseur, G., Vernieres, J., Dupuy, C. & Fabries, J. Mechanisms of mantle metasomatism: geochemical evidence from the Lherz orogenic peridotite. *J. Petrol.* **31**, 597–628 (1990).

30. Willbold, Matthias & Stracke, Andreas Trace element composition of mantle end-members: implications for recycling of oceanic and upper and lower continental crust, Geochem. *Geophys. Geosyst.* **7**, Q04004 (2006).

31. Hauri, E. H., Wagner, T. P. & Grove, T. L. Experimental and natural partitioning of Th, U, Pb and other trace elements between garnet, clinopyroxene and basaltic melts. *Chem. Geol.* **117**, 149–166 (1994).

32. Hart, S. R. & Dunn, T. Experimental cpx/melt partitioning of 24 trace elements. *Contrib. Mineral. Petrol.* **113**, 1–8 (1993).

33. Green, T. H., Blundy, J. D., Adam, J. & Yaxley, G. M. SIMS determination of trace element partition coefficients between garnet, clinopyroxene and hydrous basaltic liquids at 2–7.5 GPa and 1080–1200 °C. *Lithos* **53**, 165–187 (2000).

34. Kamenetsky, V. S., Kamenetsky, M. B., Golovin, A. V., Sharygin, V. V. & Maas, R. Ultrafresh salty kimberlite of the Udachnaya-East pipe (Yakutia, Russia): a petrological oddity or fortuitous discovery? *Lithos* **152**, 173–186 (2012).

35. Walter, M. et al. Primary carbonatite melt from deeply subducted oceanic crust. *Nature* **454**, 622–625 (2008).

36. Kim, J.-I., Choi, S. H., Koh, G. W., Park, J. B. & Ryu, J.-S. Petrogenesis and mantle source characteristics of volcanic rocks on Jeju Island, South Korea. *Lithos* **326**, 476–490 (2019).

37. Zhang, G. L. et al. Evolution of carbonated melt to alkali basalt in the South China Sea. *Nat. Geosci.* **10**, 229–235 (2017).

38. Dasgupta, R., Hirschmann, M. M. & Withers, A. C. Deep global cycling of carbon constrained by the solidus of anhydrous, carbonated eclogite under upper mantle conditions. *Earth Planet. Sci. Lett.* **227**, 73–85 (2004).

39. Matzen, A. et al. The roles of pyroxenite and peridotite in the mantle sources of oceanic basalts. *Nat. Geosci.* **10**, 530–535 (2017).

40. Mattey, D., Lowry, D. & Macpherson, C. Oxygen isotope composition of mantle peridotite. *Earth Planet. Sci. Lett.* **128**, 231–241 (1994).

41. Greenwood, R. C. et al. Oxygen isotopic evidence for accretion of Earth's water before a high-energy Moon-forming giant impact. *Sci. Adv.* **4**, eaao5928 (2018).

42. Ireland, T., Avila, J., Greenwood, R. C., Hicks, L. J. & Bridges, J. C. Oxygen isotopes and sampling of the solar system. *Space Sci. Rev.* **216**, 25 (2020).

43. Dostal, J., Zhi, X., Muehlenbachs, K., Dupuy, C. & Zhai, M. Geochemistry of Cenozoic alkali basaltic lavas from Shandong Province, eastern China. *Geochem. J.* **25**, 1–16 (1991).

44. Zeng, G., Chen, L. H., Xu, X. S., Jiang, S. Y. & Hofmann, A. W. Carbonated mantle sources for Cenozoic intra-plate alkaline basalts in Shandong, North China. *Chem. Geol.* **273**, 35–45 (2010).

45. Liu, J., Xia, Q.-K., Deloule, E., Chen, H. & Feng, M. Recycled oceanic crust and marine sediment in the source of alkali basalts in Shandong, eastern China: evidence from magma water content and oxygen isotopes. *J. Geophys. Res. Solid Earth* **120**, 8281–8303 (2015).

46. Eiler, J. M. Oxygen isotope variations of basaltic lavas and upper mantle rocks. *Rev. Mineral. Geochem.* **43**, 319–364 (2001).

47. Putirka K. D. *Minerals, Inclusions and Volcanic Processes* (Eds. Putirka, K. D. & Tepley, F. J.) 61–120. Vol 69, Reviews in Mineralogy and Geochemistry (Mineralogical Society of America, 2008)

48. Gündüz, M. & Asan, K. MagMin_PT: an Excel-based mineral classification and geothermobarometry program for magmatic rocks. *Mineral. Mag.* **87**, 1–9 (2022).

49. Petrelli, M., Caricchi, L. & Perugini, D. Machine learning thermo-barometry: application to clinopyroxene bearing magmas. *J. Geophys. Res. Solid Earth* **125**, 1–17 (2020).

50. Kil, Y., Shin, H. J., Yun, S. H., Koh, J. S. & Ahn, U. S. Geochemical characteristics of mineral phases in the mantle xenoliths from Sunheul-ri, Jeju Island. *J. Miner. Soc. Korea* **21**, 373–382 (2008).

51. Seber, D., Barazangi, M., lbenbrahimt, A. & Demnati, A. Geophysical evidence for lithospheric delamination beneath the Alboran Sea and Rif-Betic mountains. *Nature* **379**, 785–790 (1996).

52. Carlson, R. W. et al. Re-Os systematics of lithosphere peridotites: implications for lithosphere formation and preservation. In: *Proc. 7th International Kimberlite Conference* (Eds. Gurney, J. J., Gurney, J. L., Pascoe, M. D., Richardson, S. H.) 99–108. (Red Roof Design, 1999).

53. Walker, R. J., Carlson, R. W., Shirey, S. B. & Boyd, F. R. Os, Sr, Nd and Pb isotope systematics of southern African peridotite xenoliths: implications for the chemical evolution of subcontinental mantle. *Geochim. Cosmochim. Acta* **53**, 1583–1595 (1989).

54. Irvine, G. J. et al. A Re-Os isotope and PGE study of kimberlite-derived peridotite xenoliths from Somerset Island and a comparison to the Slave and Kaapvaal cratons. *Lithos* **71**, 461–488 (2003).

55. Chen, C. et al. Carbonate-rich crust subduction drives the deep carbon and chlorine cycles. *Nature* **620**, 576–581 (2023).

56. Safonov, O. G., Kamenetsky, V. S. & Perchuk, L. L. Links between carbonatite and kimberlite melts in chloride-carbonate-silicate systems: experiments and application to natural assemblages. *J. Petrol.* **52**, 1307–1331 (2011).

57. Zhang, H.-F. et al. Geochemical significance of a garnet lherzolite from the Dahongshan kimberlite, Yangtze Craton, southern China. *Geochem. J.* **35**, 315–331 (2001).

58. Allègre, C. J. & Turcotte, D. L. Implications of a two-component marble-cake mantle. *Nature* **323**, 123–127 (1986).

59. Stixrude, L. & Lithgow-Bertelloni, C. Geophysics of chemical heterogeneity in the mantle. *Annu. Rev. Earth Planet. Sci.* **40**, 569–595 (2012).

60. Kellogg, L. H. Mixing in the mantle. *Annu. Rev. Earth Planet. Sci.* **20**, 365–388 (1992).

61. Connolly, J. A. D. Computation of phase equilibria by linear programming: a tool for geodynamic modelling and its application to subduction zone decarbonation. *Earth Planet. Sci. Lett.* **236**, 524–541 (2005).

62. Holland, T. & Powell, R. Thermodynamics of order-disorder in minerals. 2. Symmetric formalism applied to solid solutions. *Am. Mineral.* **81**, 1425–1437 (1996).

63. Holland, T. J. B. & Powell, R. An internally consistent thermodynamic data set for phases of petrological interest. *J. Metamorph. Geol.* **16**, 309–343 (1998).

64. Pearce, N. J. G. et al. A compilation of new and published major and trace element data for NIST SRM 610 and NIST SRM 612 glass reference. *Mater. Geostand. Geoanal. Res.* **21**, 115–144 (1997).

65. Wessel, P., Smith, W. H. F., Scharroo, R., Luis, J. & Wobbe, F. Generic Mapping Tools: Improved version released. *EOS Trans. AGU* **94**, 409–410 (2013).

66. GEBCO compilation group. *GEBCO 2023 Grid* (2023).

67. Kim, D. et al. Helium isotopes and olivine geochemistry of basalts and mantle xenoliths in Jeju Island, South Korea: Evaluation of role of SCLM on the Cenozoic intraplate volcanism in East Asia. *Lithos* **390**, 106–123 (2021).

Author contributions

V.S., S.K., and Y.J. conceived the project. Y.K. supplied the xenolith samples for this study. V.S. performed petrographic and EPMA analyses. V.S., S.K., Y.J., K.Y., and C.P. performed LA-ICPMS and oxygen isotope analyses. Authors V.S., S.K., Y.J., Y.K., M.S., C.P., and K.Y. are arranged in order of their contributions, from highest to lowest, to the interpretation and final manuscript writing.

Competing interests

The authors declare no competing interests.

Additional information

Supplementary information The online version contains supplementary material available at https://doi.org/10.1038/s43247-023-01170-0.

Correspondence and requests for materials should be addressed to Yirang Jang.

Peer review information *Communications Earth & Environment* thanks Tomoaki Morishita, Ana Jesus, and the other, anonymous, reviewer(s) for their contribution to the peer review of this work. Primary Handling Editors: João Duarte, Joe Aslin and Aliénor Lavergne. Peer reviewer reports are available.

Reprints and permission information is available at http://www.nature.com/reprints

Publisher's note Springer Nature remains neutral with regard to jurisdictional claims in published maps and institutional affiliations.